Acta Mech 230, 771–785 (2019)
https://doi.org/10.1007/s00707-018-2281-5

ORIGINAL PAPER

S. Rashahmadi · S. A. Meguid

Modeling size-dependent thermoelastic energy dissipation of graphene nanoresonators using nonlocal elasticity theory

Received: 22 June 2018 / Revised: 7 August 2018 / Published online: 13 November 2018

Abstract Recent developments in nanostructured materials have led to the use of graphene sheets as resonators in advanced micro- and nanoelectromechanical systems. An important feature of micro- and nanoresonators is their ability to function with low power dissipation. The main intrinsic mechanism of energy loss in these advanced devices is thermoelastic damping (TED). In this article, we study TED effects in orthotropic graphene sheets of varied lengths operating at different temperatures using nonlocal elasticity theory. For this purpose, the fundamental thermoelastic relations are used to develop a system of coupled partial differential equations to describe the behavior of graphene nanoresonators. The orthotropic mechanical and thermal properties of graphene were taken into account in our model for zigzag and armchair chiralities operating at different temperatures. The free in-plane vibration of the graphene nanoresonator is analyzed using Galerkin method. Decidedly, we show that the developed system of equations is capable of describing the TED behavior of graphene nanoresonators along the two considered chiralities during thermoelastic vibration. Specifically, we examined the influence of size, chirality, and temperature upon thermoelastic damping, as measured by the so-called quality factor, of the graphene nanoresonator. Our results reveal that the nanoresonator experiences higher energy dissipation with increased temperature. They also reveal the dependence of the energy dissipation upon the size and chirality of the graphene sheet.

1 Introduction

Recent advances in micro- and nanoelectromechanical systems (MEMS/NEMS) such as mechanical nanoresonators have attracted significant attention from the scientific community. Mechanical nanoresonators are one of the most significant components of MEMS/NEMS devices. They can sense very small quantities, such as mass and force, as a result of changes in their resonance response. The performance of MEMS/NEMS can be improved by using more efficient nanoresonators that make use of low density, high flexibility, and high-strength graphene sheet [1]. In fact, graphene sheets have been considered as very suitable candidates to replace silicon in the next-generation MEMS/NEMS [2]. In recent years, extensive efforts have been dedicated to design new classes of resonators with high sensitivity, fast response, and reduced energy consumption. Reducing the energy consumption of a resonator will lead to smaller energy source. Energy consumption becomes critical, when the number of nanoresonators in an electronic device is significant. These electronic devices will be subjected to thermoelastic effects and would thus suffer from thermoelastic damping (TED) effects.

S. Rashahmadi · S. A. Meguid (✉)
Mechanics and Aerospace Design Laboratory, University of Toronto, Toronto, ON M5S 3G8, Canada
E-mail: meguid@mie.utoronto.ca

S. Rashahmadi
Department of Mechanical Engineering, Urmia University, Urmia, Iran

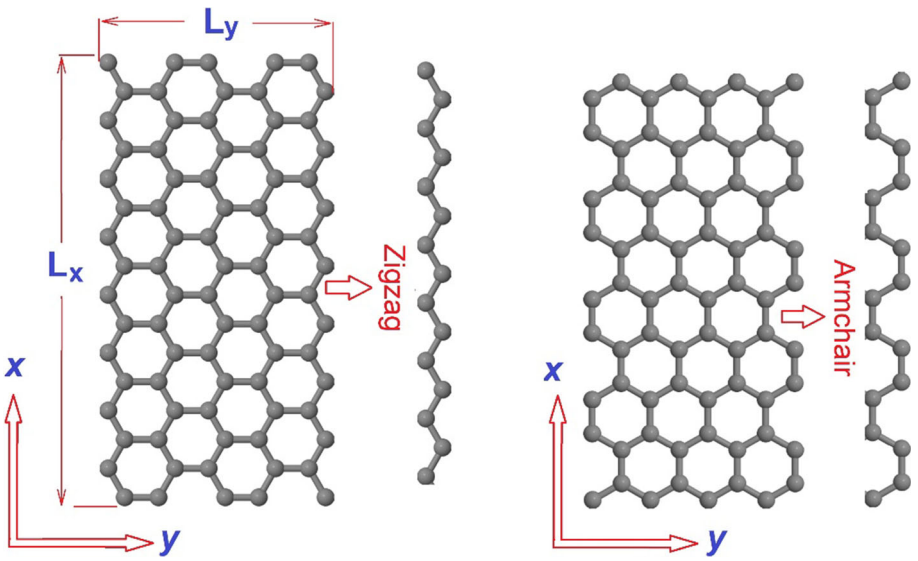

Fig. 1 A schematic of graphene nanosheet and selected zigzag and armchair chiralities

Thermoelastic damping is a mechanism which provides an insight into how energy is dissipated due to the coupling of temperature and strain in a thermoelastic solid via the thermal expansion coefficient [3,4]. Consequently, understanding TED behavior of nanostructures is a key step in the design of MEMS and NEMS devices, oscillators, gyrometers, micropumps, filters, and sensors [5–7]. The analysis of TED originated from a study by Bennewitz in 1924 [8]. Zener [9,10] identified the existence of TED as a significant dissipation mechanism in flexural resonators. The relevance of this phenomenon to MEMS was highlighted by Roszhart [6], who declared in 1990 that TED was the dominant mechanism of structural damping in vacuum-operated single-crystal silicon microresonators. Duwel et al. [11] experimentally showed that TED is the prevailing source of damping in MEMS and NEMS devices.

A number of authors used the so-called quality factor as a measure of TED dissipation. Although the Q-factor is directly related to the stored energy and the dissipation energy, it is commonly calculated using the concept of complex frequency with the aid of thermoelasticity theory. Details of the concept will be provided in Sect. 2.2. For example, a high-quality factor indicates a low level of dissipation of energy primarily by TED mechanism [3]. Lifshitz and Roukes [12] derived an analytical expression for the quality factor to study the size dependency in microbeams. Prabhakar et al. [13] presented an exact theory for TED resulting from 2-D heat conduction analysis. They deployed Green's function method to solve the 2-D heat conduction equation, and TED was derived in the form of an infinite series. Bostani and Mohammadi [14] investigated the size-dependent quality factor of thermoelastic damping in a microbeam resonator based on the modified strain gradient elasticity theory. Murmu and Pradhan [15] studied the effects of small-scale free vibration nanoplates using the theory of nonlocal continuum mechanics. Jian et al. [16] analyzed the free vibration of a single-layered graphene sheet-based mass sensor using the Galerkin strip distributed transfer function method.

The motivation behind this study is twofold. The first is concerned with energy consumption/dissipation which is one of the main issues in the design of nanoresonators. The second, as determined by the above literature, is concerned with shedding light on TED and its effect on nanostructured materials [17]. The focus of our article is to study the thermoelastic damping as determined by the quality factor of orthotropic nanoresonators using graphene sheets. Specifically, the influence of the chirality of the graphene sheet (armchair and zigzag; as depicted in Fig. 1) on TED is examined for varied lengths and operating temperatures using nonlocal elasticity theory.

2 Basic formulations of the thermoelastic behavior of graphene

2.1 Nonlocal elasticity description of a graphene nanosheet

In this study, the discrete nature of the graphene sheet is mapped into a nonlocal elastic continuum. According to Eringen [18], the stress field at a point x in a body depends not only on the strain field at the point, but also

on the strains at all neighboring points of the body. Thus, the nonlocal stress tensor components σ_{ij} at point x can be expressed as [19]:

$$\int_v k\left(\left|x'-x\right|,\tau\right)\sigma_{ij}^{l}\left(x'\right)\mathrm{d}x' \tag{1}$$

where $\sigma_{ij}^{l}\left(x'\right)$ represents the components of the classical stress tensor at point x and $k(\left|x'-x\right|,\tau)$ is the nonlocal kernel function which incorporates the small-scale effects into the constitutive equations; the nonlocal effects at the reference point x produced by local strain at the source x' has the dimension of (length)$^{-3}$. The term $\left|x'-x\right|$ represents the distance in the Euclidean space, and $\tau = e_0 a/L$ is a material constant that depends on a "characteristic length ratio/L'', where a is an internal characteristic length (e.g., lattice parameter, or distance between C–C bonds) and L is an external characteristic length (e.g., wave length, length of nanostructure). The choice of the parameter e_0 is crucial for the calibration of the nonlocal model and is typically obtained either experimentally or numerically using molecular dynamics (MD). Eringen [18] obtained a value of 0.39 for this parameter by matching the dispersion curves based on a number of atomic models [20]. The differential forms of Eq. (1) can be written as [21]:

$$\left(1-\mu\nabla^2\right)\sigma_{ij} = C_{ijkl}\varepsilon_{kl} \tag{2}$$

where σ_{ij}, ε_{kl}, and C_{ijkl} are the respective components of stress, strain, and stiffness tensors and the Laplacian $\nabla^2 = \frac{\partial^2}{\partial x^2} + \frac{\partial^2}{\partial y^2}$, which reduces to

$$\begin{aligned}
\sigma_{xx} - \mu\left(\frac{\partial^2\sigma_{xx}}{\partial x^2} + \frac{\partial^2\sigma_{xx}}{\partial y^2}\right) &= \frac{1}{1-v_x v_y}\left(E_x\varepsilon_x + v_{xy}E_y\varepsilon_y\right) - \beta_1\left(1+\varphi_1\frac{\partial}{\partial t}\right)\theta,\\
\sigma_{yy} - \mu\left(\frac{\partial^2\sigma_{yy}}{\partial x^2} + \frac{\partial^2\sigma_{yy}}{\partial y^2}\right) &= \frac{1}{1-v_x v_y}\left(v_{yx}E_x\varepsilon_x + E_y\varepsilon_y\right) - \beta_2\left(1+\varphi_1\frac{\partial}{\partial t}\right)\theta,\\
\sigma_{xy} - \mu\left(\frac{\partial^2\sigma_{xy}}{\partial x^2} + \frac{\partial^2\sigma_{xy}}{\partial y^2}\right) &= G_{xy}\varepsilon_{xy}
\end{aligned} \tag{3}$$

for a graphene nanosheet which is considered under plane stress condition. In the above expressions,

$$\beta_1 = \frac{1}{1-v_x v_y}\left(E_x\alpha_x + v_{xy}E_y\alpha_y\right), \quad \beta_2 = \frac{1}{1-v_x v_y}\left(v_{yx}E_x\alpha_x + E_y\alpha_y\right) \quad \text{and} \quad \theta = T - T_0 \tag{4}$$

with φ_1 being the mechanical relaxation time, E_x and E_y are Young's moduli, v_x and v_y are Poisson's ratios, and α_x and α_y are the thermal expansion coefficients in the x and y directions, respectively. In addition, T and T_0 are the respective initial and final temperatures, and G_{xy} is the shear modulus of graphene. A graphene sheet with length $L_x(0 \le x \le L_x)$, width $L_y(0 \le y \le L_y)$, and thickness h is considered in the current study; (see Fig. 1).

The small strain–displacement relations for plane stress can be expressed as:

$$\varepsilon_x = \frac{\partial u}{\partial x}, \quad \varepsilon_y = \frac{\partial v}{\partial y}, \quad \gamma_{xy} = \frac{1}{2}\left(\frac{\partial u}{\partial y} + \frac{\partial v}{\partial x}\right), \quad \varepsilon_{zz} = \gamma_{xz} = \gamma_{yz} = 0. \tag{5}$$

In rectangular Cartesian coordinates (x, y), the equations of motion can be written as:

$$\sigma_{ij,j-}\rho a_i = 0. \tag{6}$$

Substituting Eq. (5) into Eq. (3) and substituting the result into Eq. (6) yields the governing equation of motion, viz:

$$\begin{aligned}
&\left(C_{11}\frac{\partial^2 u}{\partial x^2} + C_{12}\frac{\partial^2 v}{\partial x\partial y}\right) - v_1\left(\frac{\partial\theta}{\partial x} + \varphi_1\frac{\partial^2\theta}{\partial x\partial t}\right) + C_{66}\left(\frac{\partial^2 v}{\partial x\partial y} + \frac{\partial^2 u}{\partial y^2}\right) - \rho\frac{\partial^2 u}{\partial t^2}\\
&+ \rho\mu\left(\frac{\partial^4 u}{\partial x^2\partial t^2} + \frac{\partial^4 u}{\partial y^2\partial t^2}\right) = 0,
\end{aligned} \tag{7}$$

$$\begin{aligned}
&\left(C_{21}\frac{\partial^2 u}{\partial x\partial y} + C_{22}\frac{\partial^2 v}{\partial y^2}\right) - v_2\left(\frac{\partial\theta}{\partial y} + \varphi_1\frac{\partial^2\theta}{\partial y\partial t}\right) + C_{66}\left(\frac{\partial^2 v}{\partial x^2} + \frac{\partial^2 u}{\partial x\partial y}\right) - \rho\frac{\partial^2 v}{\partial t^2}\\
&+ \rho\mu\left(\frac{\partial^4 v}{\partial x^2\partial t^2} + \frac{\partial^4 v}{\partial y^2\partial t^2}\right) = 0.
\end{aligned} \tag{8}$$

2.2 Thermoelastic damping model

The equation of heat conduction for an orthotropic plate can be expressed as follows [22]:

$$T_{,ii} = \frac{2\rho c_p}{\delta_1 + \delta_2}\frac{\partial}{\partial t}\left(1 + \varphi_2\frac{\partial}{\partial t}\right)T + \frac{T_0\,(\beta_1 + \beta_2)}{\delta_1 + \delta_2}\frac{\partial}{\partial t}\left(1 + \varphi_2\delta\frac{\partial}{\partial t}\right)u_{i,i} \quad i = 1, 2 \tag{9}$$

where $\delta_j = \alpha_j c_p \rho (j = 1, 2)$ are the coefficients of thermal conductivity, c_p is the specific heat per unit mass, ρ is the density, δ is the Kronecker delta, and φ_2 is the mechanical relaxation time. In the nonabbreviated form, Eq. (9) can be expressed as

$$\frac{\partial^2 T}{\partial x^2} + \frac{\partial^2 T}{\partial y^2} = \frac{2c_p}{\delta_1 + \delta_2}\frac{\partial}{\partial t}\left(1 + \varphi_2\frac{\partial}{\partial t}\right)T + \frac{T_0\,(\beta_1 + \beta_2)}{\delta_1 + \delta_2}\frac{\partial}{\partial t}\left(1 + \varphi_2\frac{\partial}{\partial t}\right)\left(\frac{\partial u}{\partial x} + \frac{\partial v}{\partial y}\right). \tag{10}$$

Let us now introduce the so-called quality factor which is defined as the ratio of the stored energy in the microstructure U to the dissipated energy ΔU [12], viz:

$$Q = 2\pi\frac{U}{\Delta U}. \tag{11}$$

Energy loss mechanisms can be classified into two types: (i) extrinsic losses which can be altered by changing the design or the operating conditions of MEMS. Air damping and support losses are examples of the main contributing extrinsic losses, and (ii) Intrinsic losses which are associated with the operation of the resonators in which TED typically imposes an upper limit on the reachable quality factor.

Noteworthy is the fact that thermoelastic damping is a mechanism of structural damping in which energy is dissipated due to irreversible heat conduction within a vibrating thermoelastic structure. According to the complex frequency approach, Q_{TED} can be calculated as [12]

$$Q_{\mathrm{TED}} = \frac{1}{2}\left|\frac{\mathrm{Re}\,(\Omega)}{\mathrm{Im}\,(\Omega)}\right| \tag{12}$$

where $\mathrm{Re}\,(\Omega)$ is the real part and $\mathrm{Im}\,(\Omega)$ is the imaginary part of the complex frequency. For the sake of clarity, we have provided a simple derivation of the quality factor in "Appendix 1" using a single degree of freedom of a spring–mass system under dynamic loading. Further details can be obtained in Refs. [12,14,23,24].

Equations (7), (8), and (10) represent a system of coupled differential equations which will be used to analyze the nanoresonator in-plane vibration and the associated TED. Adopting the following nondimensional parameters in the above equations:

$$\hat{x} = \frac{x}{a}, \quad \hat{y} = \frac{y}{b}, \quad \hat{u} = \frac{u}{a}, \quad \hat{v} = \frac{v}{b}, \quad \hat{\theta} = \frac{\theta}{T_0}, \quad \hat{t} = \frac{t}{t_0}, \quad \hat{w}_0 = \frac{w_0}{h}, \quad t_0^2 = \frac{a^2\rho}{C_{11}} \tag{13}$$

leads to the following normalized equations:

$$\left(C_{11}\frac{\partial^2\hat{u}}{a\partial\hat{x}^2} + C_{12}\frac{\partial^2\hat{v}}{a\partial\hat{x}\partial\hat{y}}\right) - v_1\left(\frac{T_0\partial\hat{\theta}}{a\partial\hat{x}} + \varphi_1\frac{T_0\partial^2\hat{\theta}}{at_0\partial\hat{x}\partial\hat{t}}\right) + C_{66}\left(\frac{a\partial^2\hat{u}}{b^2\partial\hat{y}^2} + \frac{\partial^2\hat{v}}{a\partial\hat{x}\partial\hat{y}}\right) - \rho\frac{a\partial^2\hat{u}}{t_0^2\partial\hat{t}^2}$$
$$+\frac{\rho\mu}{t_0^2\partial\hat{t}^2}\left(\frac{\partial^4\hat{u}}{a\partial\hat{x}^2} + \frac{a\partial^4\hat{u}}{b^2\partial\hat{y}^2}\right) = 0, \tag{14}$$

$$\left(C_{21}\frac{\partial^2\hat{u}}{b\partial\hat{x}\partial\hat{y}} + C_{22}\frac{\partial^2\hat{v}}{b\partial\hat{y}^2}\right) - v_2\left(\frac{T_0\partial\hat{\theta}}{b\partial\hat{y}} + \varphi_1\frac{T_0\partial^2\hat{\theta}}{bt_0\partial\hat{y}\partial\hat{t}}\right) + C_{66}\left(\frac{\partial^2\hat{u}}{b\partial\hat{x}\partial\hat{y}} + \frac{b\partial^2\hat{v}}{a^2\partial\hat{x}^2}\right) - \rho\frac{b\partial^2\hat{v}}{t_0^2\partial\hat{t}^2}$$
$$+\frac{\rho\mu}{t_0^2\partial\hat{t}^2}\left(\frac{b\partial^4\hat{v}}{a^2\partial\hat{x}^2} + \frac{\partial^4\hat{v}}{b\partial\hat{y}^2}\right) = 0, \tag{15}$$

$$\left(\frac{\partial^2}{a^2\partial\hat{x}^2} + \frac{\partial^2}{b^2\partial\hat{y}^2}\right)\left(T_0\hat{\theta}\right) - \frac{2\rho c_p}{\delta_1 + \delta_2}\frac{\partial}{t_0\partial\hat{t}}\left(1 + \varphi_2\frac{\partial}{t_0\partial\hat{t}}\right)T_0\hat{\theta} - \frac{T_0\,(v_1 + v_2)}{\delta_1 + \delta_2}\frac{\partial}{t_0\partial\hat{t}}$$
$$\left(1 + \varphi_2\delta\frac{\partial}{t_0\partial\hat{t}}\right)\left(\frac{\partial\hat{u}_0}{\partial\hat{x}} + \frac{\partial\hat{v}_0}{\partial\hat{y}}\right) = 0 \tag{16}$$

where the details of the constant C_{ij} are provided in "Appendix 2."

3 Numerical solution

In order to solve the coupled governing Eqs. (14–16), Galerkin method is applied, and the complex frequency of free vibration of the nanosheet resonator is extracted. Based on this approach, the displacements and temperature can be approximated using linear combinations of appropriate shape functions and time-dependent coefficients, such that:

$$\hat{u}\left(\hat{x},\hat{y},\hat{t}\right)=\sum_{n=1}^{N}\sum_{m=1}^{M}\beta_n\left(\hat{x}\right)\beta_m\left(\hat{y}\right)a_{mn}\left(\hat{t}\right), \tag{17}$$

$$\hat{v}\left(\hat{x},\hat{y},\hat{t}\right)=\sum_{k=1}^{K}\sum_{f=1}^{F}\gamma_k\left(\hat{x}\right)\gamma_f\left(\hat{y}\right)b_{kf}\left(\hat{t}\right), \tag{18}$$

$$\hat{\theta}\left(\hat{x},\hat{y},\hat{t}\right)=\sum_{i=1}^{I}\sum_{j=1}^{J}\emptyset_i\left(\hat{x}\right)\emptyset_j\left(\hat{y}\right)d_{ij}\left(\hat{t}\right). \tag{19}$$

A suitable shape function should be chosen to satisfy the geometrical boundary conditions of the nanosheet such that

$$\begin{aligned}
\beta_n\left(\hat{x}\right)&=Sin\left(n\pi\hat{x}\right), \qquad \beta_m\left(\hat{y}\right)=Sin\left(m\pi\hat{y}\right),\\
\gamma_k\left(\hat{x}\right)&=Sin\left(k\pi\hat{x}\right), \qquad \gamma_f\left(\hat{y}\right)=Sin\left(f\pi\hat{y}\right),\\
\emptyset_i\left(\hat{x}\right)&=Sin\left(i\pi\hat{x}\right), \qquad \emptyset_j\left(\hat{y}\right)=Sin\left(j\pi\hat{y}\right).
\end{aligned} \tag{20}$$

By substituting Eqs. (17), (18), and (19) into Eqs. (14), (15), and (16), the following error functions are obtained:

$$\begin{aligned}
&B_1\sum_{n=1}^{N}\sum_{m=1}^{M}\beta_n''\left(\hat{x}\right)\beta_m\left(\hat{y}\right)a_{mn}\left(\hat{t}\right)+B_2\sum_{k=1}^{K}\sum_{f=1}^{F}\gamma_k'\left(\hat{x}\right)\gamma_f'\left(\hat{y}\right)b_{kf}\left(\hat{t}\right)\\
&-B_3\sum_{i=1}^{I}\sum_{j=1}^{J}\emptyset_i'\left(\hat{x}\right)\emptyset_j\left(\hat{y}\right)d_{ij}\left(\hat{t}\right)-B_4\sum_{i=1}^{I}\sum_{j=1}^{J}\emptyset_i'\left(\hat{x}\right)\emptyset_j\left(\hat{y}\right)\dot{d}_{ij}\left(\hat{t}\right)\\
&+B_5\sum_{n=1}^{N}\sum_{m=1}^{M}\beta_n\left(\hat{x}\right)\beta_m''\left(\hat{y}\right)a_{mn}\left(\hat{t}\right)+B_6\sum_{k=1}^{K}\sum_{f=1}^{F}\gamma_k'\left(\hat{x}\right)\gamma_f'\left(\hat{y}\right)b_{kf}\left(\hat{t}\right)\\
&-B_7\sum_{n=1}^{N}\sum_{m=1}^{M}\beta_n\left(\hat{x}\right)\beta_m\left(\hat{y}\right)\ddot{a}_{mn}\left(\hat{t}\right)+B_8\sum_{n=1}^{N}\sum_{m=1}^{M}\beta_n''\beta_m\left(\hat{y}\right)\ddot{a}_{mn}\left(\hat{t}\right)\\
&+B_9\sum_{n=1}^{N}\sum_{m=1}^{M}\beta_n\left(\hat{x}\right)\beta_m''\left(\hat{y}\right)\ddot{a}_{mn}\left(\hat{t}\right)=\epsilon_1,
\end{aligned} \tag{21}$$

$$\begin{aligned}
&D_1\sum_{n=1}^{N}\sum_{m=1}^{M}\beta_n'\left(\hat{x}\right)\beta_m'\left(\hat{y}\right)a_{mn}\left(\hat{t}\right)+D_2\sum_{k=1}^{K}\sum_{f=1}^{F}\gamma_k\left(\hat{x}\right)\gamma_f''\left(\hat{y}\right)b_{kf}\left(\hat{t}\right)\\
&-D_3\sum_{i=1}^{I}\sum_{j=1}^{J}\emptyset_i\left(\hat{x}\right)\emptyset_j'\left(\hat{y}\right)d_{ij}\left(\hat{t}\right)-D_4\sum_{i=1}^{I}\sum_{j=1}^{J}\emptyset_i\left(\hat{x}\right)\emptyset_j'\left(\hat{y}\right)\dot{d}_{ij}\left(\hat{t}\right)\\
&+D_5\sum_{n=1}^{N}\sum_{m=1}^{M}\beta_n'\left(\hat{x}\right)\beta_m'\left(\hat{y}\right)a_{mn}\left(\hat{t}\right)+D_6\sum_{k=1}^{K}\sum_{f=1}^{F}\gamma_k''\left(\hat{x}\right)\gamma_f\left(\hat{y}\right)b_{kf}\left(\hat{t}\right)
\end{aligned}$$

$$
\begin{aligned}
&- D_7 \sum_{k=1}^{K} \sum_{f=1}^{F} \gamma_k(\hat{x})\, \gamma_f(\hat{y})\, \ddot{b}_{kf}(\hat{t}) + D_8 \sum_{k=1}^{K} \sum_{f=1}^{F} \gamma_k''(\hat{x})\, \gamma_f(\hat{y})\, \ddot{b}_{kf}(\hat{t}) \\
&+ D_9 \sum_{k=1}^{K} \sum_{f=1}^{F} \gamma_k(\hat{x})\, \gamma_f''(\hat{y})\, \ddot{b}_{kf}(\hat{t}) = \epsilon_2, \qquad (22)
\end{aligned}
$$

$$
\begin{aligned}
&k_1 \sum_{i=1}^{I} \sum_{j=1}^{J} \emptyset_i''(\hat{x})\, \emptyset_j(\hat{y})\, d_{ij}(\hat{t}) + k_2 \sum_{i=1}^{I} \sum_{j=1}^{J} \emptyset_i(\hat{x})\, \emptyset_j''(\hat{y})\, d_{ij}(\hat{t}) \\
&-k_3 \sum_{i=1}^{I} \sum_{j=1}^{J} \emptyset_i(\hat{x})\, \emptyset_j(\hat{y})\, \dot{d}_{ij}(\hat{t}) - k_4 \sum_{i=1}^{I} \sum_{j=1}^{J} \emptyset_i(\hat{x})\, \emptyset_j(\hat{y})\, \ddot{d}_{ij}(\hat{t}) \\
&- k_5 \sum_{n=1}^{N} \sum_{m=1}^{M} \beta_n'(\hat{x})\, \beta_m(\hat{y})\, \dot{a}_{mn}(\hat{t})) - k_6 \sum_{k=1}^{K} \sum_{f=1}^{F} \gamma_k(\hat{x})\, \gamma_f'(\hat{y})\, \dot{b}_{kf}(\hat{t}) \\
&- k_7 \sum_{n=1}^{N} \sum_{m=1}^{M} \beta_n'(\hat{x})\, \beta_m(\hat{y})\, \ddot{a}_{mn}(\hat{t}) - k_8 \sum_{k=1}^{K} \sum_{m=1}^{M} \gamma_k(\hat{x})\, \gamma_f'(\hat{y})\, \ddot{b}_{kf}(\hat{t}) = \epsilon_3 \qquad (23)
\end{aligned}
$$

where $B_w, D_w, k_y, w = 1\ldots9, y = 1\ldots8$ are constants which are provided in "Appendix 2."

According to Galerkin weighted residual method, the following conditions should be satisfied:

$$\int_0^1 \int_0^1 \beta_p(\hat{x})\, \beta_q(\hat{y})\, \epsilon_1 \mathrm{d}\hat{x}\mathrm{d}\hat{y} = 0 \quad p = 1, \ldots, N \quad q = 1, \ldots, M, \qquad (24)$$

$$\int_0^1 \int_0^1 \gamma_g(\hat{x})\, \gamma_h(\hat{y})\, \epsilon_2 \mathrm{d}\hat{x}\mathrm{d}\hat{y} = 0 \quad g = 1, \ldots, K \quad h = 1, \ldots, F, \qquad (25)$$

$$\int_0^1 \int_0^1 \emptyset_s(\hat{x})\, \emptyset_z(\hat{y})\, \epsilon_3 \mathrm{d}\hat{x}\mathrm{d}\hat{y} = 0 \quad s = 1, \ldots, I \quad z = 1, \ldots, J. \qquad (26)$$

By substituting Eq. (20) into Eqs. (24–26) and simplifying them using the dominant terms of the displacements as well as the dominant terms of the heat conducted in x and y directions, the following equations are obtained:

$$(B_{5a} + B_{1a}) a_{11}(\hat{t}) - B_{3a} d_{21}(\hat{t}) + (B_{8a} - B_{7a} + B_{9a})\, \ddot{a}_{11}(\hat{t}) = 0, \qquad (27)$$

$$(D_{2a} + D_{6a}) b_{11}(\hat{t}) + (D_{8a} - D_{7a} + D_{9a})\, \ddot{b}_{11}(\hat{t}) = 0, \qquad (28)$$

$$(K_{1a} + K_{2a})\, d_{21}(\hat{t}) - K_{3a} \dot{d}_{21}(\hat{t}) - K_{5a} \dot{a}_{11}(\hat{t}) = 0. \qquad (29)$$

The coefficients B_{1a}, B_{3a}, B_{5a}, B_{8a}, D_{2a}, $D6a$, D_{8a}, K_{1a}, K_{2a}, and K_{5a} are provided in "Appendix 3."

By considering $a_{11}(\hat{t}) = \alpha_{11} e^{\Omega \hat{t}}$, $b_{11}(\hat{t}) = \beta_{11} e^{\Omega \hat{t}}$, and $d_{21}(\hat{t}) = \gamma_{21} e^{\Omega \hat{t}}$ and substituting them into Eqs. (27–29), the complex frequencies are obtained, and according to the complex frequency approach, Q_{TED} can be calculated from Eq. (12). In "Appendix 4", we highlight the approach adopted in solving the above coupled system of equations.

4 Results and discussion

4.1 Mechanical and thermal properties of graphene

It should be noted that the mechanical properties of a graphene sheet are orthotropic, temperature- and size-dependent [25]. In this regard, the material properties, including Young's modulus, shear modulus, Poisson's ratio, thermal expansion coefficients, and effective thickness of a graphene sheet, need to be carefully determined since they are needed for the TED model.

Two types of graphene sheets were examined in this study (zigzag and armchair), as illustrated in Fig. 1. Different operating temperatures (300 K, 500 K, and 700 K) were considered. The effective thickness was calculated as per the formulations outlined in [26]. The mechanical and thermal properties for the examined graphene sheets are listed in Table 1 [27]. In addition, the density of graphene was taken to be 2200 kg/m^3 [16], and the specific heat per unit mass (c_p) was assumed to be 700 J/K kg [28].

Table 1 Material properties of graphene sheet obtained from MD simulation [27]

Temperature	$T_0 = 300$ K	500 K	700 K
Type 1: zigzag graphene plate, $L_x = 21.8391$ nm, $L_y = 4.8976$ nm, $h = 0.0801$ nm			
Elasticity modulus, E_x (GPa)	3559	3508	3495
Elasticity modulus, E_y (GPa)	3521	3483	3370
Shear modulus, G_{xy} (GPa)	1523	1523	1685
Poisson's ratio, υ_{xy}	0.205	0.205	0.205
Poisson's ratio, υ_{yx}	0.202	0.202	0.202
Coefficient of thermal expansion, $\alpha_x (10^{-6}\,\mathrm{K}^{-1})$	1.833	2.016	2.252
Coefficient of thermal expansion, $\alpha_y (10^{-6}\,\mathrm{K}^{-1})$	1.316	1.819	2.111
Type 2: armchair graphene plate, $L_x = 21.9131$ nm, $L_y = 4.895$ nm, $h = 0.0744$ nm			
Elasticity modulus, E_x (GPa)	3886	3790	3763
Elasticity modulus, E_y (GPa)	3967	3911	3830
Shear modulus, G_{xy} (GPa)	1775	1653	1680
Poisson's ratio, υ_{xy}	0.192	0.192	0.192
Poisson's ratio, υ_{yx}	0.196	0.196	0.196
Coefficient of thermal expansion, $\alpha_x (10^{-6}\,\mathrm{K}^{-1})$	1.583	1.735	2.022
Coefficient of thermal expansion, $\alpha_y (10^{-6}\,\mathrm{K}^{-1})$	2.164	2.259	2.34

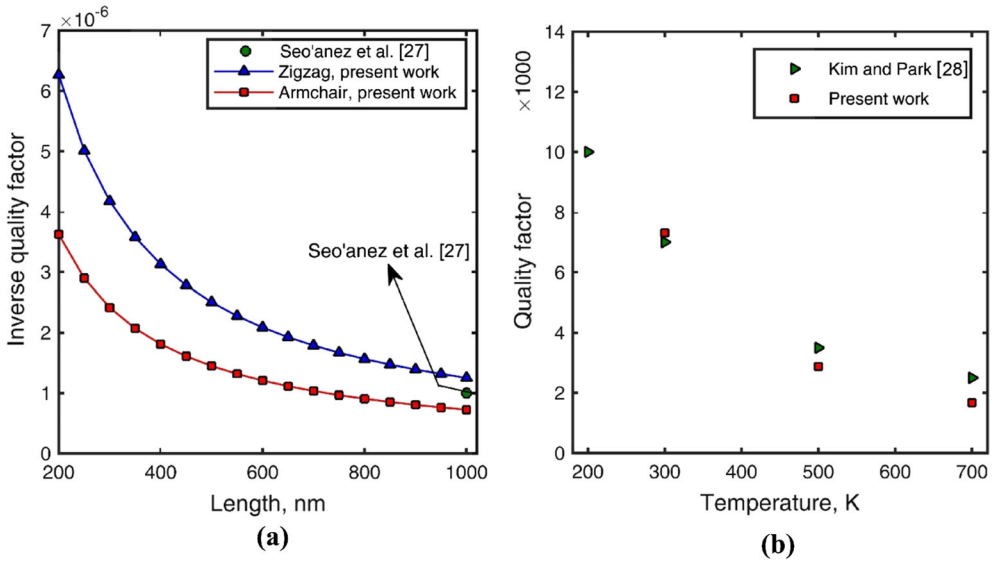

Fig. 2 Comparison of our model predictions with: **a** the experimental work of Seoànez et al. [29] and **b** the molecular dynamics simulations of Kim and Park [30] for $\frac{e_0 a}{L} = 0.1$

4.2 Model validation and selection of nonlocal parameters

The quality factor results obtained from our model were validated with the works of Seoànez et al. [29] and Kim and Park [30]. Seoàanez et al. [29] experimentally estimated that Q^{-1}–10^{-6} at 300 K for a length of 1 μm, and Kim and Park [30] used classical MD to study the effects of energy dissipation in graphene monolayers for a circular graphene monolayer with a diameter of 56.8 Å. As shown in Fig. 2, our predictions are in close agreements with their experimental findings and MD simulations.

Figure 3 illustrates the effect of the nonlocal parameters $\frac{e_0 a}{L}$ on the quality factor for different sheet lengths (10–30 nm) and (100–500 nm) at a temperature of 300 K for zigzag-type chirality. The Figure also shows that the quality factor is influenced by the selection of the nonlocal parameter. In order to show the effect of the nonlocal parameter on the quality factor, we used the commonly adopted nonlocal parameters $\frac{e_0 a}{L} \approx 0.1$–$0.6$ [20].

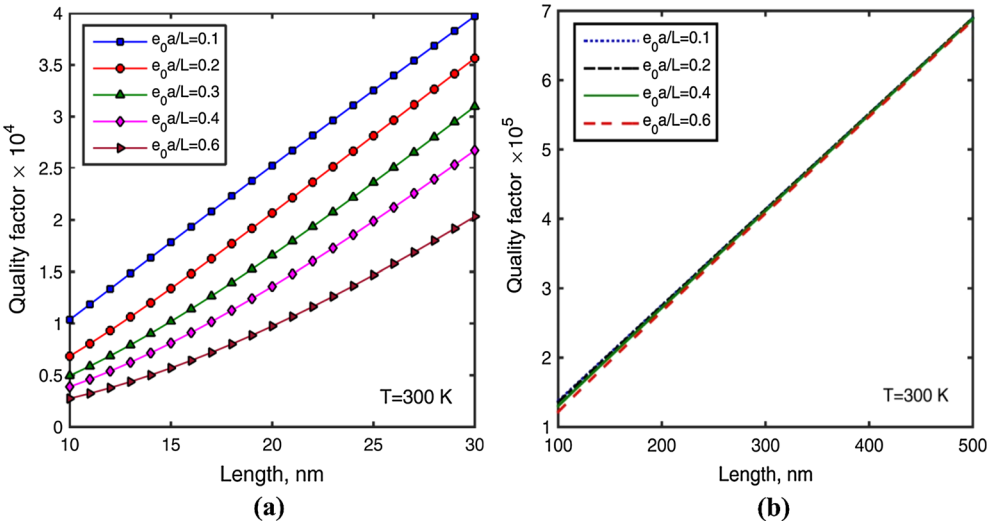

Fig. 3 Effect of nonlocal parameters on the quality factor for different sheet lengths: **a** 10–30 nm, **b** 100–500 nm at an operating temperature of 300 K for zigzag–type chirality

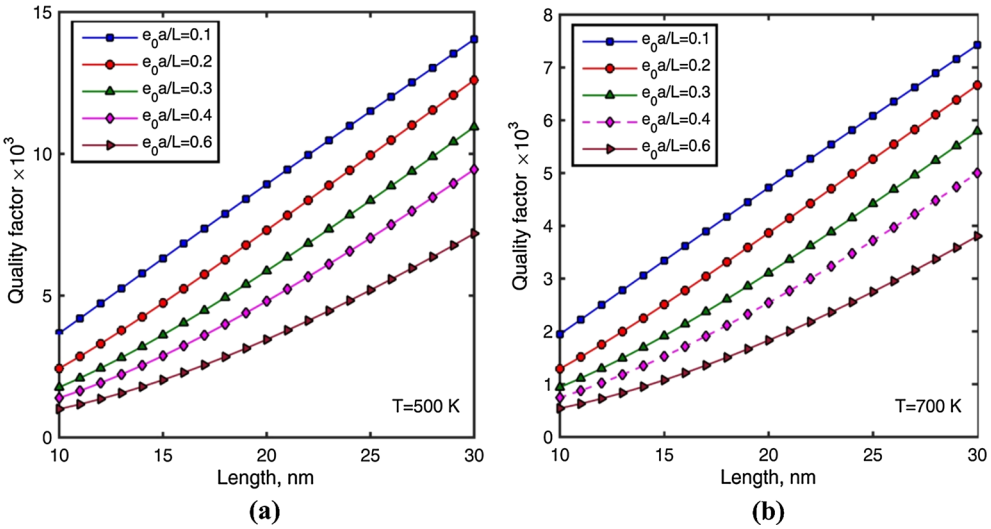

Fig. 4 Variation of quality factor versus sheet lengths at different temperatures: **a** 500 K and **b** 700 K for zigzag-type chirality

4.3 Effect of the governing parameters on the quality factor for zigzag-type chirality

In order to study the effect of temperature, the quality factor of the graphene sheet was determined for higher operating temperatures for zigzag-type chirality (500–700 K). Figure 4a shows the variation of the quality factor for a temperature of 500 K, while Fig. 4b shows it for a temperature of 700 K versus sheet lengths for varied nonlocal parameters. Comparison of the results between Figs. 3 and 4 shows that increasing the temperature of the graphene sheet leads to a decrease in the quality factor; i.e., more energy dissipation during the operation of the nanoresonator. It also shows that a decrease in the nonlocal parameter could lead to a dramatic decrease in the quality factor. For example, when $\frac{e_0 a}{L} = 0.1$ and a graphene sheet length of 30 nm with an operating temperature of 300 K, the quality factor is around 39,720, while at $\frac{e_0 a}{L} = 0.6$, it is approximately half of that value (20,334); indicative of the importance of the proper selection of the nonlocal parameter. As indicated in the validation Section, comparison of the results of our study with the literature reveals that the selection of a nonlocal parameter $\frac{e_0 a}{L} = 0.1$ is appropriate.

Furthermore, as Figs. 3 and 4 show, increasing the graphene sheet length leads to a higher quality factor. Our results for $T = 300$ K show that the quality factor increases with the increase in the sheet length from

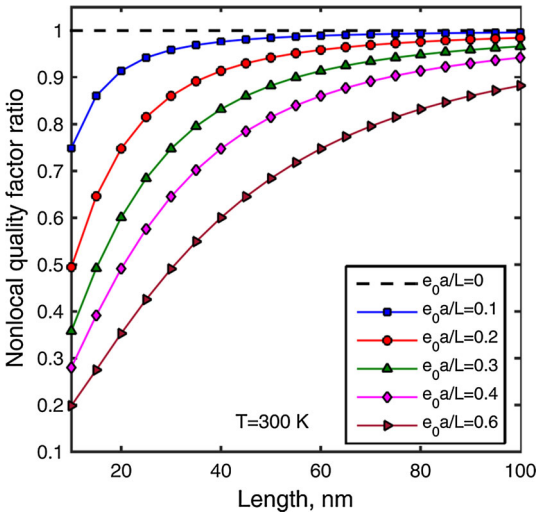

Fig. 5 Nonlocal quality factor ratio (QR $= Q^{\mathrm{NL}}/Q^{L}$) versus sheet length at a temperature of 300 K for zigzag-type chirality

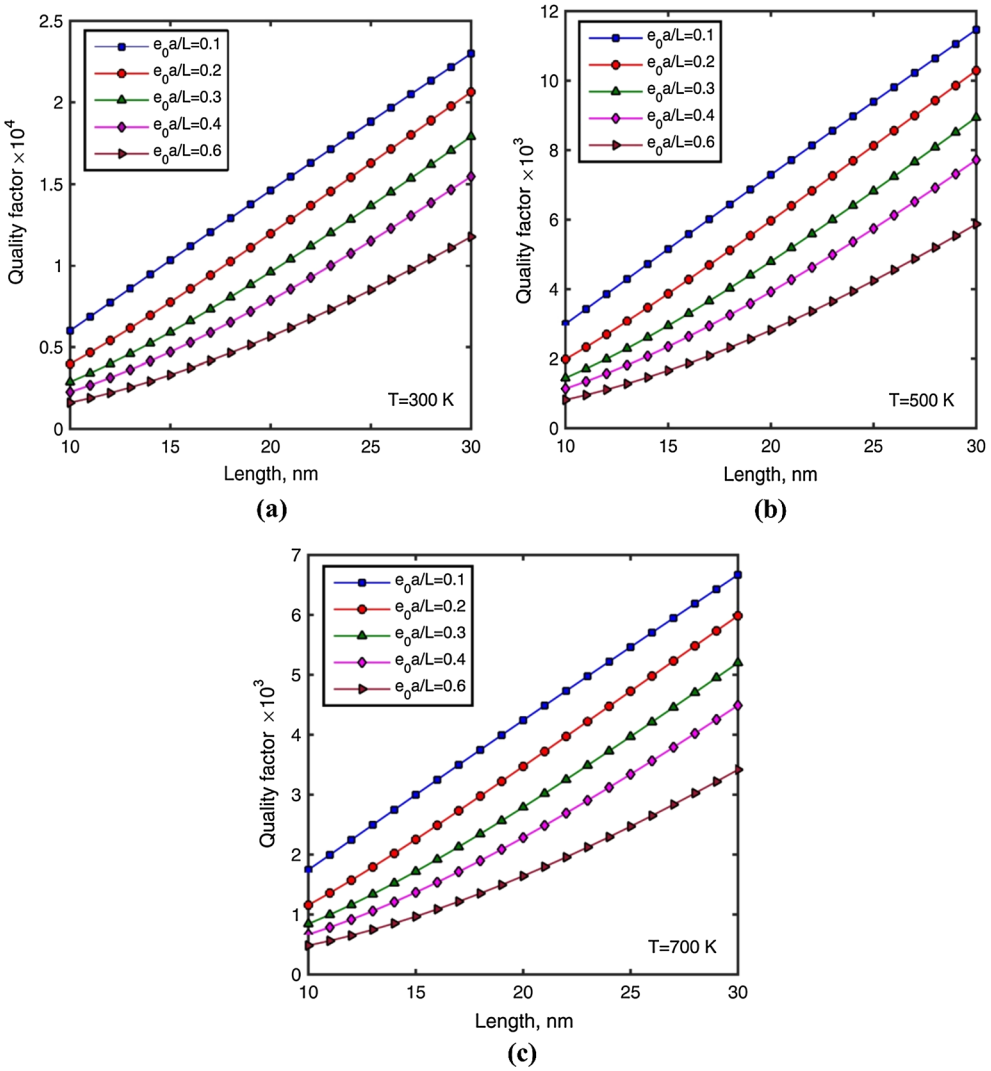

Fig. 6 Variation of quality factor versus sheet length for armchair-type chirality at different temperatures: **a** 300 K, **b** 500 K, and **c** 700 K

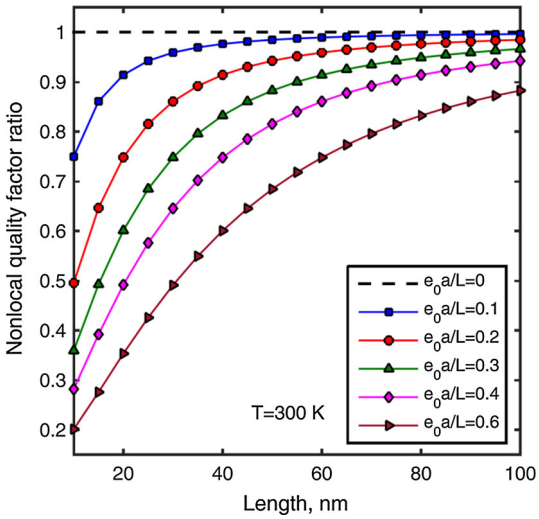

Fig. 7 Nonlocal quality factor ratio (QR $= Q^{\mathrm{NL}}/Q^{L}$) at temperature 300 K and sheet length 10–100 nm for armchair-type chirality

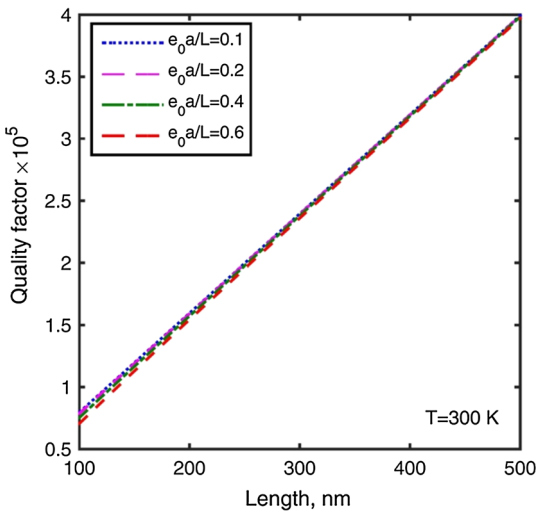

Fig. 8 Effect of nonlocal parameters on the quality factor for sheet length (100–500 nm) for armchair-type chirality at a temperature of 300 K

10^4 for the smallest sheet length (10 nm) to 3.9×10^4 for the largest sheet length considered in our study (30 nm). For example, in the case of 10 nm sheet length with an increase in temperature from 300 K to 500 K, the quality factor decreased by 63%; this decrease is only 47% when the operating temperature increases from 500 K to 700 K. Interestingly, our results also show that the effect of the nonlocal parameter on the results diminishes with the increase in the sheet length beyond 100 nm, as shown in Fig. 3b.

It is worth noting that in the limit when $\frac{e_0 a}{L} \rightarrow 0$, the quality factor approaches the classical theory of elasticity. This can be further explained via the use of the nonlocal quality factor ratio which is the ratio of the nonlocal quality factor to the classical continuum theory factor, viz., $\left(\mathrm{QR} = \frac{Q^{\mathrm{NL}}}{Q^{L}}\right)$. Unlike the local quality factor, the nonlocal quality factor is a quality factor in which the nonlocal theory of elasticity has been adopted to account for small-scale effects. The small-scale effects play an important role in energy dissipation. Figure 5 shows the variation of this ratio for different sheet lengths at a temperature of 300 K for zigzag-type chirality. The Figure shows that the difference between the nonlocal and the classical analyses results decreases with the increase in the length of the graphene sheet.

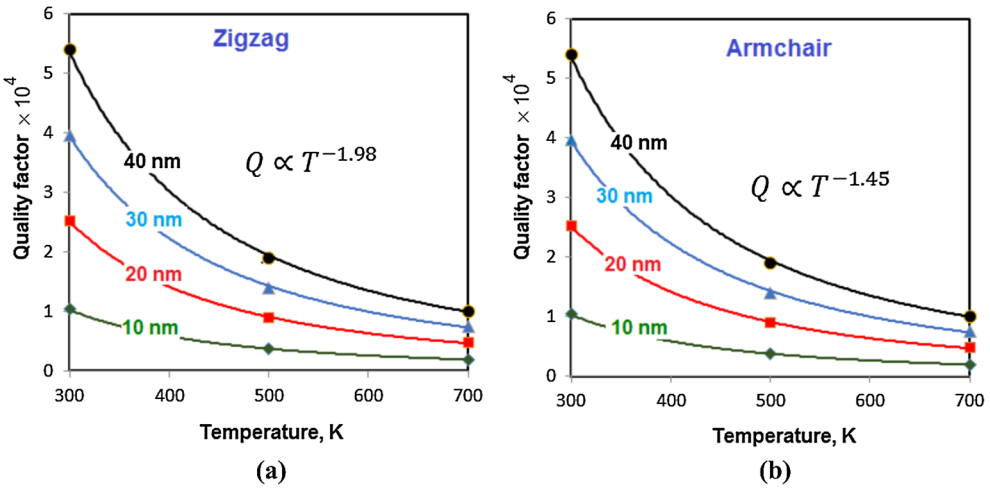

Fig. 9 Rate of change of quality factor versus temperature for different sheet lengths: **a** zigzag-type and **b** armchair-type chirality

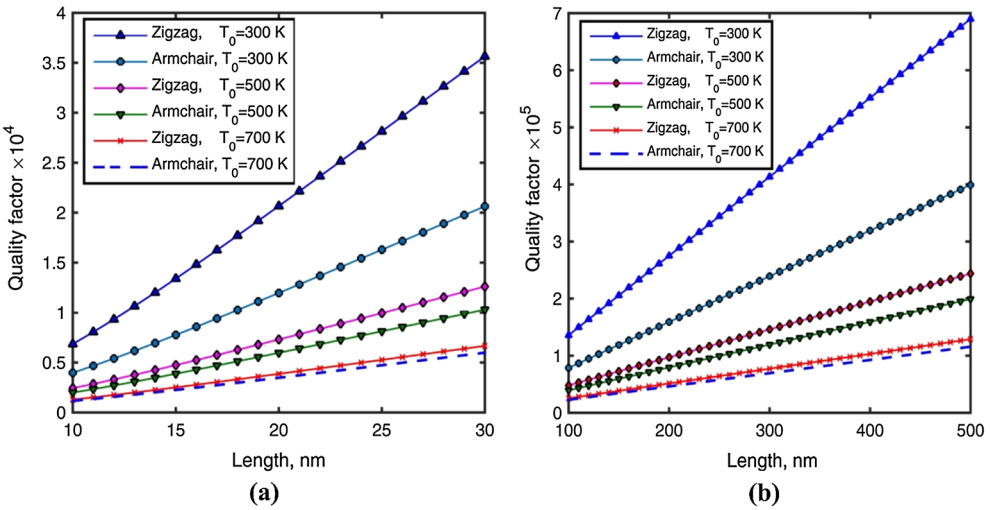

Fig. 10 Comparison of quality factors for zigzag and armchair-type chirality under different operating temperatures with nonlocal parameter = 0.1 for varied sheet length: **a** 10–30 nm, and **b** 100–500 nm graphene sheet length

In summary, our results reveal that the quality factor is inversely proportional to temperature. Furthermore, it indicates that the intrinsic losses can be reduced significantly across a range of operating temperatures by increasing the length of the graphene resonator.

4.4 Effect of the governing parameters on the quality factor for armchair-type chirality

As for armchair-type chirality, Fig. 6a–c shows the change in the quality factor versus the length of the graphene sheet that is subjected to operating temperature of 300 K, 500 K, and 700 K, and varied nonlocal parameters. Our predictions indicate that for both zigzag and armchair-types chiralities, the quality factor decreases as the operating temperature increases, but the rate of change versus length is different for these types of chiralities. For example, for a graphene sheet of length 20 nm, the respective quality factors for armchair are approximately 14,600, 7290, and 4240 for 300 K, 500 K, and 700 K. The reduction from 14,600 to 7290 and from 7290 to 4240 corresponds to a respective reduction of 50% and 42% which relate to the increase in their respective temperature ratios of 166% and 140%.

Figure 7 shows the variation of the normalized quality factor $\frac{Q^{NL}}{Q^{L}}$ ratio for sheet lengths 20–100 nm, and Fig. 8 shows the variation of the same quality factor for sheet lengths between 100 and 500 nm operating at a temperature of 300 K for armchair-type chirality. The variation in the quality factor for armchair chirality is comparable to those observed using zigzag-type chirality.

In Fig. 9, the rate of change of the quality factor versus temperature is presented for different sheet lengths. We observe that the respective quality factors are found to be proportional to $T^{-1.98}$ for zigzag and $T^{-1.45}$ for armchair-type chirality. This indicates that the reduction rate in the quality factor and consequently the corresponding increase in the dissipated energy due to temperature is higher for zigzag-type chirality.

Figure 10a, b provides a comparison of the quality factor in these two types of graphene sheets. Although there is no serious difference between zigzag and armchair layouts in terms of TED, the quality factors for zigzag-type chirality are higher than for the armchair chirality in each operating temperature. The difference between the quality factors of zigzag and armchair chirality is about 40%, 18%, and 10% when subjected to operating temperatures of 300 K, 500 K, and 700 K, respectively. These results are depicted in Fig. 9 for graphene sheets of lengths of 10–30 nm and in Fig. 10 for graphene lengths of 100–500 nm.

5 Conclusions

In order to examine TED in graphene sheets, we developed fundamental thermoelastic relations in the form of a coupled system of partial differential equations that are capable of describing the behavior of graphene as nanoresonator of varied lengths subject to different operating temperatures. Additionally, the orthotropic mechanical and thermal properties of graphene sheets loaded along zigzag and armchair-type chirality were considered. The free in-plane vibration of the graphene nanoresonator was analyzed using Galerkin method. Specifically, we examined the influence of length, chirality of the graphene sheet, and operating temperature upon the quality factor of graphene nanoresonators. Our results reveal that increasing the length and temperature of the graphene sheet leads to a higher quality factor implying an increase in the effective energy dissipation of the nanoresonator. The respective rate of reduction of the quality factor is approximately 63% and 47% for zigzag-type chirality and 50% and 42% for armchair which correspond to an increase in the operating temperature from 300 K to 500 K and from 500 K to 700 K, respectively. Our results further reveal that the respective quality factor reduction rate is proportional to $T^{-1.98}$ for zigzag and $T^{-1.45}$ for armchair-type chirality. In addition, the quality factor for zigzag-type is slightly higher than for armchair-type chirality for all operating temperatures considered in this study. This quality factor difference between zigzag and armchair is about 40%, 18%, and 10% for operating temperatures of 300 K, 500 K, and 700 K, respectively.

Acknowledgements The authors wish to thank the Natural Sciences and Engineering Research Council of Canada for the partial financial support of the current investigations. S. Rashahmadi wishes to thank the Department of Mechanical Engineering and Urmia University, Urmia, Iran, for approving his sabbatical leave at the University of Toronto, Canada.

Appendix 1

As a simple example, let us determine the Q-factor for a single degree of freedom mass–spring system whose governing equation has the form:

$$\ddot{x} + 2\varsigma\omega_0\dot{x} + \omega_0^2 \mathrm{x} = 0 \text{ with } \varsigma = \frac{\mathrm{c}}{2\sqrt{\mathrm{km}}},\ \omega_0 = \sqrt{\mathrm{k/m}} \tag{A1.1}$$

where x is the displacement of the mass, $1/2\varsigma$ is the Q-factor of the system [1], ω_0 denotes the natural frequency, c is the damping coefficient, and k and m are spring stiffness and mass, respectively. By assuming x = f (x) $e^{i\omega t}$, and substituting it into above equation, one obtains:

$$\omega^2 - i.\left(2\varsigma\omega_0\omega\right) - (\omega_0^2)x = 0. \tag{A1.2}$$

Note that $i = \sqrt{-1}$. Solving the above quadratic expression, one gets:

$$\omega = \left(\sqrt{1-\varsigma^2} + i.\varsigma\right)\omega_0. \tag{A1.3}$$

The Q-factor is defined in terms of the above complex frequency as being:

$$Q = \frac{1}{2\varsigma} \approx \frac{\sqrt{1-\varsigma^2}}{2\varsigma} = \frac{\mathrm{Re}\,(\omega)}{2\,\mathrm{Im}\,(\omega)}. \tag{A1.4}$$

Correspondingly, the dissipation is the inverse of the quality factor and is denoted as:

$$Q^{-1} = 2\left|\frac{\mathrm{Im}\,(\omega)}{\mathrm{Re}\,(\omega)}\right|. \tag{A1.5}$$

The above expressions are adopted in our article to investigate the TED of nanoscale devices, and the detailed derivations are provided in Refs. [2–4].

Appendix 2

$$C_{11} = \frac{E_x}{\left(1-v_{xy}v_{yx}\right)}, \quad C_{22} = \frac{E_y}{\left(1-v_{xy}v_{yx}\right)}, \quad C_{12} = \frac{v_{yx}E_x}{\left(1-v_{xy}v_{yx}\right)} = \frac{v_{xy}E_y}{\left(1-v_{xy}v_{yx}\right)},$$
$$C_{66} = \frac{G_{xy}}{2}, \quad B_1 = \frac{C_{11}}{a} \quad B_2 = \frac{C_{12}}{a}, \quad B_3 = \frac{T_0 v_1}{a} \quad B_4 = \frac{T_0 v_1 \varphi_1}{a t_0},$$
$$B_5 = \frac{aC_{66}}{b^2}, \quad B_6 = \frac{C_{66}}{a}, \quad B_7 = \frac{\rho a}{t_0^2}, \quad B_8 = \frac{\rho\mu}{a t_0^2} \quad B_9 = \frac{\rho\mu a}{b^2 t_0^2}, \quad D_1 = \frac{C_{21}}{b},$$
$$D_2 = \frac{C_{22}}{b}, \quad D_3 = \frac{T_0 v_2}{b}, \quad D_4 = \frac{T_0 v_2 \varphi_1}{b t_0}, \quad D_5 = \frac{C_{66}}{b}, \quad D_6 = \frac{bC_{66}}{a^2}, \quad D_7 = \frac{\rho b}{t_0^2}, \quad D_8 = \frac{\rho\mu b}{a^2 t_0^2},$$
$$D_9 = \frac{\rho\mu}{b t_0^2}, \quad k_1 = \frac{T_0}{a^2}, \quad k_2 = \frac{T_0}{b^2}, \quad k_3 = \frac{2T_0\rho c_p}{t_0(\delta_1+\delta_2)}, \quad k_4 = \frac{2T_0 c_p s\varphi_2}{t_0^2(\delta_1+\delta_2)},$$
$$k_5 = \frac{T_0\left(v_1+v_2\right)}{t_0(\delta_1+\delta_2)}, \quad k_6 = \frac{T_0\left(v_1+v_2\right)}{t_0(\delta_1+\delta_2)}, \quad k_7 = \frac{\delta T_0\left(v_1+v_2\right)\varphi_2}{t_0^2(\delta_1+\delta_2)}, \quad k_8 = k_7.$$

Appendix 3

$$B_{1a} = B_1\int_0^1\int_0^1 \beta_p\left(\hat{x}\right)\beta_q\left(\hat{y}\right)\beta_n''\left(\hat{x}\right)\beta_m\left(\hat{y}\right)\mathrm{d}\hat{x}\mathrm{d}\hat{y}, \quad B_{3a} = B_3\int_0^1\int_0^1 \beta_p\left(\hat{x}\right)\beta_q\left(\hat{y}\right)\emptyset_i'\left(\hat{x}\right)\emptyset_j\left(\hat{y}\right)\mathrm{d}\hat{x}\mathrm{d}\hat{y},$$
$$B_{5a} = B_5\int_0^1\int_0^1 \beta_p\left(\hat{x}\right)\beta_q\left(\hat{y}\right)\beta_n\left(\hat{x}\right)\beta_m''\left(\hat{y}\right)\mathrm{d}\hat{x}\mathrm{d}\hat{y}, \quad B_{7a} = B_7\int_0^1\int_0^1 \beta_p\left(\hat{x}\right)\beta_q\left(\hat{y}\right)\beta_n\left(\hat{x}\right)\beta_m\left(\hat{y}\right)\mathrm{d}\hat{x}\mathrm{d}\hat{y},$$
$$B_{8a} = B_8\int_0^1\int_0^1 \beta_p\left(\hat{x}\right)\beta_q\left(\hat{y}\right)\beta_n''\left(\hat{x}\right)\beta_m\left(\hat{y}\right)\mathrm{d}\hat{x}\mathrm{d}\hat{y}, \quad B_{9a} = B_9\int_0^1\int_0^1 \beta_p\left(\hat{x}\right)\beta_q\left(\hat{y}\right)\beta_n\left(\hat{x}\right)\beta_m''\left(\hat{y}\right)\mathrm{d}\hat{x}\mathrm{d}\hat{y},$$
$$D_{2a} = D_2\int_0^1\int_0^1 \gamma_g\left(\hat{x}\right)\gamma_h\left(\hat{y}\right)\gamma_k\left(\hat{x}\right)\gamma_f''\left(\hat{y}\right)\mathrm{d}\hat{x}\mathrm{d}\hat{y}, \quad D_{6a} = D_6\int_0^1\int_0^1 \gamma_g\left(\hat{x}\right)\gamma_h\left(\hat{y}\right)\gamma_k''\left(\hat{x}\right)\gamma_f\left(\hat{y}\right)\mathrm{d}\hat{x}\mathrm{d}\hat{y},$$
$$D_{7a} = D_7\int_0^1\int_0^1 \gamma_g\left(\hat{x}\right)\gamma_h\left(\hat{y}\right)\gamma_k\left(\hat{x}\right)\gamma_f\left(\hat{y}\right)\mathrm{d}\hat{x}d\hat{y}, \quad D_{8a} = D_8\int_0^1\int_0^1 \gamma_g\left(\hat{x}\right)\gamma_h\left(\hat{y}\right)\gamma_k''\left(\hat{x}\right)\gamma_f\left(\hat{y}\right)\mathrm{d}\hat{x}\mathrm{d}\hat{y},$$
$$K_{1a} = K_1\int_0^1\int_0^1 \emptyset_s\left(\hat{x}\right)\emptyset_z\left(\hat{y}\right)\emptyset_i''\left(\hat{x}\right)\emptyset_j\left(\hat{y}\right)\mathrm{d}\hat{x}\mathrm{d}\hat{y}, \quad K_{2a} = K_2\int_0^1\int_0^1 \emptyset_s\left(\hat{x}\right)\emptyset_z\left(\hat{y}\right)\emptyset_i\left(\hat{x}\right)\emptyset_j''\left(\hat{y}\right)\mathrm{d}\hat{x}\mathrm{d}\hat{y},$$
$$K_{3a} = K_3\int_0^1\int_0^1 \emptyset_s\left(\hat{x}\right)\emptyset_z\left(\hat{y}\right)\emptyset_i\left(\hat{x}\right)\emptyset_j\left(\hat{y}\right)\mathrm{d}\hat{x}\mathrm{d}\hat{y}, \quad K_{5a} = K_5\int_0^1\int_0^1 \emptyset_s\left(\hat{x}\right)\emptyset_z\left(\hat{y}\right)\beta_m\left(\hat{y}\right)\beta_n'\left(\hat{x}\right)\mathrm{d}\hat{x}\mathrm{d}\hat{y}.$$

Appendix 4

In order to solve the coupled thermoelastic Eqs. (27–29), we assumed that a_{11}, b_{11} and d_{21} take the following form:

$$a_{11}\left(\hat{\mathrm{t}}\right) = \alpha_{11}e^{\Omega\hat{\mathrm{t}}}, b_{11}\left(\hat{\mathrm{t}}\right) = \beta_{11}e^{\Omega\hat{t}} \text{ and } d_{21}\left(\hat{t}\right) = \gamma_{21}e^{\Omega\hat{\mathrm{t}}} \tag{A4.1}$$

where:

$$\Omega = \mathrm{Re}\left(\Omega\right) + \mathrm{iIm}\left(\Omega\right), \tag{A4.2}$$

and substituting them into Eqs. (27–29), the complex frequencies can be obtained as follows:

$$\begin{bmatrix} (B_{5a}+B_{1a})+\Omega^2\left(D_{8a}-D_{7a}+D_{9a}\right) & 0 & -B_{3a} \\ 0 & (D_{2a}+D_{6a})+\Omega^2\left(D_{8a}-D_{7a}+D_{9a}\right) & 0 \\ -\Omega K_{5a} & 0 & (K_{1a}+K_{2a})-\Omega K_{3a} \end{bmatrix} \begin{Bmatrix} a_{11} \\ b_{11} \\ d_{21} \end{Bmatrix} = 0, \tag{A4.3}$$

and therefore:

$$\det \begin{bmatrix} (B_{5a}+B_{1a})+\Omega^2\left(D_{8a}-D_{7a}+D_{9a}\right) & 0 & -B_{3a} \\ 0 & (D_{2a}+D_{6a})+\Omega^2\left(D_{8a}-D_{7a}+D_{9a}\right) & 0 \\ -\Omega K_{5a} & 0 & (K_{1a}+K_{2a})-\Omega K_{3a} \end{bmatrix} = 0, \tag{A4.4}$$

and according to the complex frequency approach, Q_{TED} can be calculated from Eq. (12).

References

1. Oshidari, Y., Hatakeyama, T., Kometani, R., Warisawa, S., Ishihara, S.: High quality factor graphene resonator fabrication using resist shrinkage-induced strain. Appl. Phys. Express **5**, 117201 (2012)
2. Jiang, R.W., Shen, Z.B., Tang, G.J.: A semi-analytical method for nonlocal buckling and vibration of a single-layered graphene sheet nanomechanical resonator subjected to initial in-plane loads. Acta Mech. **228**, 1725–1734 (2017)
3. Yu, J.Y., Tian, X.G., Liu, J.: Size-dependent damping of a nanobeam using nonlocal thermoelasticity: extension of Zener, Lifshitz, and Roukes' damping model. Acta Mech. **228**, 1287–1302 (2017)
4. Nourmohammadi, Z.: Thermoelastic damping in micromechanical and nanomechanical resonators. Department of Mechanical Engineering, PhD Thesis, McGill University, Montreal, Quebec (2014)
5. Nayfeh, A.H., Younis, M.I.: Modeling and simulations of thermoelastic damping in microplates. J. Micromech. Microeng. **4**, 1711–1717 (2004)
6. Roszhart, T.V.: Proceedings of the Solid-State Sensor and Actuator Workshop. Hilton Head Island, SC, IEEE, New York (1990)
7. Vahdat, A.S., Rezazadeh, G., Ahmadi, G.: Thermoelastic damping in a micro-beam resonator tunable with piezoelectric layers. Acta Mech. Solida Sin. **25**, 73–81 (2012)
8. Severine, L.: Stochastic finite element method for the modeling of thermoelastic damping in microresonators. Ph.D., Department of Aerospace and Mechanics, University of Liege (2006)
9. Zener, C.: Internal friction in solids I, theory of internal friction in reeds. Phys. Rev. **52**, 230–235 (1937)
10. Zener, C.: Internal friction in solids II, general theory of thermoelastic internal friction. Phys. Rev. **53**, 90–99 (1938)
11. Duwel, A., Gorman, J., Weinstein, M., Borenstein, J., Ward, P.: Experimental study of thermoelastic damping in MEMS gyros. Sensors Actuators A Phys. **103**, 70–75 (2003)
12. Lifshitz, R., Roukes, M.L.: Thermoelastic damping in micro-and nanomechanical systems. Phys. Rev. B **61**, 5600–5609 (2000)
13. Prabhakar, S., Vengallatore, S.: Theory of thermoelastic damping in micromechanical resonators with two-dimensional heat conduction. J. Microelectromech. Syst. **17**, 494–502 (2008)
14. Bostani, M., Karami Mohammadi, A.: Thermoelastic damping in microbeam resonators based on modified strain gradient elasticity and generalized thermoelasticity theories. Acta Mech. **229**, 173–192 (2018)
15. Murmu, T., Pradhan, S.: Small-scale effect on the free in-plane vibration of nanoplates by nonlocal continuum model. Physica E Low Dimens. Syst. Nanostruct. **41**, 1628–1633 (2009)
16. Jiang, R.W., Shen, Z.B., Tang, G.J.: Vibration analysis of a single-layered graphene sheet-based mass sensor using the Galerkin strip distributed transfer function method. Acta Mech. **227**, 2899–2910 (2016)
17. Wallbank, J.: Electronic Properties of Graphene Heterostructures with Hexagonal Crystals. Springer, New York (2014)
18. Eringen, A.C.: Nonlocal Continuum Field Theories. Springer, New York (2002)
19. Despotovic, N.: Stability and vibration of a nanoplate under body force using nonlocal elasticity theory. Acta Mech. **229**, 273–284 (2018)

20. Tiwari, A., Balandin, A.A. (eds.): Innovative Graphene Technologies: Evaluation and Applications, vol. 2. Smithers Rapra Technology Ltd., Akron (2013)
21. Ansari, R., Shahabodini, A., Rouhi, H.: A nonlocal plate model incorporating interatomic potentials for vibrations of graphene with arbitrary edge conditions. Curr. Appl. Phys. **15**, 1062–1069 (2015)
22. Abd-Alla, A., Abo-Dahab, S., Hammad, H.: Propagation of Rayleigh waves in generalized magneto-thermoelastic orthotropic material under initial stress and gravity field. Appl. Math. Model. **35**, 2981–3000 (2011)
23. Casiano M.J.: Extracting damping ratio from dynamic data and numerical solutions. Marshall Space Flight Center, Huntsville, Alabama, NASA/TM-218227 (2016)
24. Yi, Y.B.: Geometric effects on themoelastic damping in MEMS resonators. J. Sound Vib. **309**, 588–599 (2008)
25. Lee, C., Wei, X., Kysar, J.W., Hone, J.: Measurement of the elastic properties and intrinsic strength of monolayer graphene. Science **321**, 385–388 (2008)
26. Huang, Y., Wu, J., Hwang, K.C.: Thickness of graphene and single-wall carbon nanotubes. Phys. Rev. B **74**, 245413 (2006)
27. Xu, Y., Shen, H., Li Zhang, C.: Nonlocal plate model for nonlinear bending of bilayer graphene sheets subjected to transverse loads in thermal environments. Compos. Struct. **98**, 294–302 (2013)
28. Pop, E., Varshney, V., Roy, A.K.: Thermal properties of graphene: fundamentals and applications. MRS Bull. **37**, 1273–1281 (2012)
29. Seoànez, C., Guinea, F., Castro Neto, A.H.: Dissipation in graphene and nanotube resonators. Phys. Rev. B **76**, 125427 (2007)
30. Kim, S.Y., Park, H.S.: Multilayer friction and attachment effects on energy dissipation in graphene nanoresonators. Appl. Phys. Lett. **94**, 101918 (2009)